Biomacromolecules

Article

Cite This: Biomacromolecules 2019, 20, 1288−1296

pubs.acs.org/Biomac

Nanostructural Properties and Twist Periodicity of Cellulose Nanofibrils with Variable Charge Density

Mario Arcari,[†] Elena Zuccarella,[†] Robert Axelrod,[†] Jozef Adamcik,[†] Antoni Sánchez-Ferrer,[†] Raffaele Mezzenga,*[,†,‡] and Gustav Nyström*[,†,§]

[†]ETH Zurich, Department of Health Sciences and Technology, Schmelzbergstrasse 9, LFO E23, 8092, Zurich, Switzerland

[‡]ETH Zurich, Department of Materials, Wolfgang-Pauli-Strasse 10, 8093 Zurich, Switzerland

[§]EMPA, Laboratory for Cellulose & Wood Materials, Überlandstrasse 129, 8600 Dübendorf, Switzerland

Supporting Information

ABSTRACT: Cellulose nanofibrils (CNFs) are a renewable and facile to produce nanomaterial that recently gained a lot of attention in soft material research. The nanostructural properties of the fibrils largely determine their self-organizing functionalities, and the ability to tune the CNF nanostructure through control of the processing parameters is therefore crucial for developing new applications. In this study, we systematically altered the CNF production parameters (i.e., variation in cellulose source, chemical, and mechanical treatment) to observe their impact on the nanostructural properties of the resulting fibrils. Atomic force microscopy (AFM) allowed detailed topological examination of individual CNFs to elucidate fibril properties such as contour length, kink distribution and the right-handed twist periodicity of individual fibrils. Statistical analysis revealed a large dependency of the fibril properties on the industrial treatment of the cellulose source material. Our results furthermore confirm that the average charge density of the fibrils regulates both contour length and twist periodicity and, thus, has a very strong impact on the final morphology of CNFs. These results provide a route to tune the detailed nanostructure of CNFs with potential impact on the self-organization of these biological colloids and their optimal use in new nanomaterials.

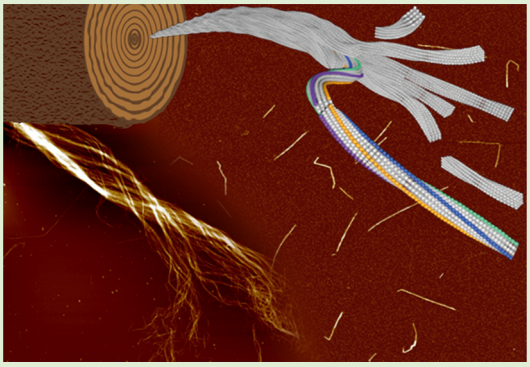

Due to its exceptional mechanical properties, nanofibrillated cellulose is a source for a multitude of applications such as material reinforcement, hydrogels, liquid crystals and aerogels production.[1,2] The mechanical quality of native cellulose originates from the multiple hydrogen bonds that strongly link the individual cellulose CNFs within cellulose bundles that reinforce plant cell walls. This intricate hydrogen bonded matrix, including also additional biopolymers (i.e., lignin and hemicellulose), provides impressive reinforcement properties in the native state, but also complicates the process to individually separate the single fibrils for new applications. One possible route to obtain NFC consists of the use of an enzymatic pretreatment, followed by mechanical homogenization or sonication.[3−5] However, the fibrils resulting from this process are typically very polydisperse in thickness, organized in bundles of single fibrils, and measuring ∼5−90 nm in width.

Saito et al. presented an elegant way to obtain individualized CNFs from wood pulp using TEMPO-mediated oxidation conditions at pH 10 (T-CNF).[6] This process allowed the production of well-defined single nanofibrils at high yields, opening up for a variety of applications to evolve, such as transparent films for food packaging with improved oxygen barriers,[7−9] free-standing hydrogels with only 0.1 wt % cellulose mass fraction,[10] and aerogels with potential as lightweight thermal insulators.[11] Due to their high surface area, nanocellulose aerogels can further be applied as absorbents for environmental remediation[12] or as templates for batteries.[13]

Worldwide, various groups work with the above-mentioned TEMPO protocol to make different material sources accessible and compare properties of diverse nanofibrillated cellulose with T-CNF,[14−19] where surface modifications is of special interest. Due to the mild conditions of the TEMPO-mediated oxidation process and the high selectivity to oxidize the methylene C6 carbon on the surface of the CNF, the crystalline fibril core is largely preserved.[14] Alternative to the faster TEMPO-mediated oxidation at pH 10 using NaClO as primary oxidant, resulting in a low number of residual aldehydes at the C6 carbon, there is the slower oxidation at neutral pH with $NaClO_2$, preventing the formation of aldehydes and minimizing the change in the degree of polymerization of the underlying cellulose chains.[20] Moreover, it has been shown that increasing the charge density of T-CNF by increasing the amounts of hypochlorite as primary oxidant

Received: November 29, 2018
Revised: January 21, 2019
Published: January 23, 2019

DOI: 10.1021/acs.biomac.8b01706
Biomacromolecules 2019, 20, 1288−1296

leads to shorter fibrils.[21] Varying the exposition to sonication was also found to influence yield, diameter, and degree of polymerization of CNF.[17,18]

Usov et al. suggested that kinks, present along the contour of CNFs, result from the processing conditions, therefore, caused by the sonication treatment and not from alternating amorphous and crystalline domains along the nanofibril.[19,22] The mechanism of breaking fibrils was also shown in a very recent study, where it was found that fibrils break preferably within rigid segments rather than at positions of kinks as one might assume.[23] These results are in agreement with Saito et al., who compared fibrils with various sonication times and additionally observed that the length of T-CNF converges toward a minimum of 278 ± 127 nm after more than 60 min of sonication for fibrils with a carboxylate content of 1.5 mmol per gram of oxidized wood cellulose.[24]

Nanocellulose particles are furthermore known to twist, as experimentally observed on microfibrils[25] and aggregated cellulose nanocrystals.[26,27] These results from higher order nanocellulose structures were supported by observations of the twist on single CNFs,[19] all cases revealing a right-handed twist. This right-handed twisted configuration has been confirmed by theoretical simulations as the lowest energy state for native, uncharged, crystalline CNFs.[28,29] The amount of twist resulting from the simulations was independent of the length of the fibrils,[30,31] but inversely dependent on the fibril cross-section area,[30−32] generally demonstrating a twisting of ∼1.5 to 10 deg/nm for different fibril thicknesses.[30,31] Even though there is a consensus about the right-handed twisted nature of CNFs, a direct experimental analysis of the twist periodicity of single CNFs is still missing. The exact mechanism behind the twisting also remains debated, specifically the role of the hydrogen bonds[33] and the influences of crystalline distortions induced by mechanical defects in the form of kinks.[34] Another unknown, yet highly relevant, parameter is the influence on the twist periodicity of the type and amount of charges introduced by surface modification during nanocellulose production.

Investigating the prior literature, there is a lack of a clear picture of the combined influence of mechanical (sonication) and chemical (pulp chemistry, charge density) treatments on the nanostructure and twist periodicity of T-CNF. Systematically altering production parameters and mapping out the impact of the manufacturing process on the CNF nanostructure in a single study becomes even more important in the context of the recent published work of Schütz et al., where they showed that variations in cellulose sources may lead to tremendously different properties of the resultant cellulose nanocrystals.[35]

In this paper, we systematically studied the change in fibril properties as a result of variations in sonication time of TEMPO-mediated oxidized CNFs with different charge densities produced from industrially bleached and unbleached softwood pulp. AFM imaging provided a basis to obtain statistics of the CNF contours including information about contour length, kinks, the average segment length, height, and fibril twist. Dynamic light scattering (DLS) and wide-angle X-ray scattering (WAXS) were used as complementary techniques to benchmark the average contour lengths and the diameter of the crystallites obtained from AFM.

We found that different charge densities (induced by varying the oxidation treatment) and different sonication times affect the fibril length and periodicity of the twist. These results contribute to our understanding of how the processing conditions can be used to control the CNF nanostructure, thus providing a tunability that is crucial for the use of CNFs in high performance applications.

EXPERIMENTAL SECTION

All materials and devices used are listed in the Supporting Information.

Synthesis of Carboxylated Cellulose Nanofibrils. Carboxylated CNF were prepared from bleached and unbleached commercial never-dried sulphite softwood-dissolving pulp (Domsjö, Sweden) by TEMPO-mediated oxidation at pH 10.[6] Thereby, the amount of NaClO as oxidation agent was varied between 1.5 up to 10 mmol/g of cellulose in order to obtain pulps with different charge densities. The oxidized cellulose pulp was dispersed in 100 mL of Milli-Q water (0.5 g/L), ultrasonicated (operated at 200 W, 24 kHz, no interval, 20% amplitude, 7 mm probe) for various durations up to 25 min, followed by centrifugation at 4000 RCF for 45 min to remove nonfibrillated cellulose aggregates.

Measurement of Charge Density. The charge density was determined by conductivity titration on the oxidized cellulose pulp fibers following the protocol SCAN-CM 65:02. The fibers were dispersed in Milli-Q water to obtain a total volume of 500 mL with a NaCl concentration of 1 mM. The pH was adjusted to 2.5 and stirred for 30 min to protonate all carboxyl groups. The dispersion was thereafter titrated adding NaOH up to pH 10 while the conductivity was recorded. The charge density of the carboxyl groups was then readily obtained from the plateau region of conductivity.

Fibril Characterization Using Atomic Force Microscopy (AFM). The freshly cleaved mica was modified with 20 μL of 0.05% (3-aminopropyl)triethoxysilane (APTES) for 60 s to induce positive charges on the surface. A droplet of around 2 mg/L fibril dispersion was deposited on the mica and allowed to adsorb for 30 s before it was rinsed with Milli-Q water and dried with pressurized air. The AFM measurements were conducted in tapping mode under ambient conditions using commercial cantilevers (Bruker) to obtain images with a resolution of at least 2.9 nm/pixel. To prevent selectivity for only charged particles, control experiments without APTES modification of the mica were also performed (Figure S7).

The images were analyzed with FiberApp,[36] where only single fibrils were considered. In addition, agglomerates and fibrils that showed splitting events were not considered (see SI for further experimental details).

Earlier AFM measurements revealed that the height of CNF's are in the range of 2−6 nm.[15,16,19] Since the tip radius (∼8 nm) is larger than the fibrils, the width on the AFM image represents predominantly the tip geometry itself and not the width of the fibrils; therefore, only the height values are included in the analysis.[37]

The analysis of the twist periodicity was performed with the height distribution tool implemented in FiberApp, where for each sample 40 straight fibril segments were tracked and the periodicity determined by the average distance between local maxima along to the fibril contour. The standard error was calculated from the variation of the periodicity between these 40 fibrils.

Wide-Angle X-ray Scattering (WAXS). Wide-angle X-ray scattering (WAXS) experiments were performed using a Rigaku MicroMax-002$^+$ equipped with a microfocused beam (40 W, 45 kV, 0.88 mA) with the $\lambda_{CuK\alpha}$ = 0.15418 nm radiation collimated by three pinhole collimators (0.4, 0.3, and 0.8 mm) in order to obtain direct information on the scattering patterns. The WAXS intensity was collected by a two-dimensional Fujifilm BAS-MS 2025 imaging plate system (15.2 × 15.2 cm^2, 50 μm resolution). An effective scattering vector range of 0.05 nm^{-1} < q < 25 nm^{-1} was obtained, where q is the scattering wave vector defined as $q = 4\pi \sin\theta/\lambda_{CuK\alpha}$ with a scattering angle of 2θ.

The average axial and radial crystallite dimensions were calculated from the correlation length (ξ) obtained by deconvoluting the WAXS intensity profile (Figure S8). Specifically, the correlation length (ξ) of both q_{004} and q_{020} peaks were evaluated from the corresponding full width half maxima (fwhm) following the relation $\xi = \frac{2\pi}{\text{fwhm}}$.

DOI: 10.1021/acs.biomac.8b01706
Biomacromolecules 2019, 20, 1288−1296

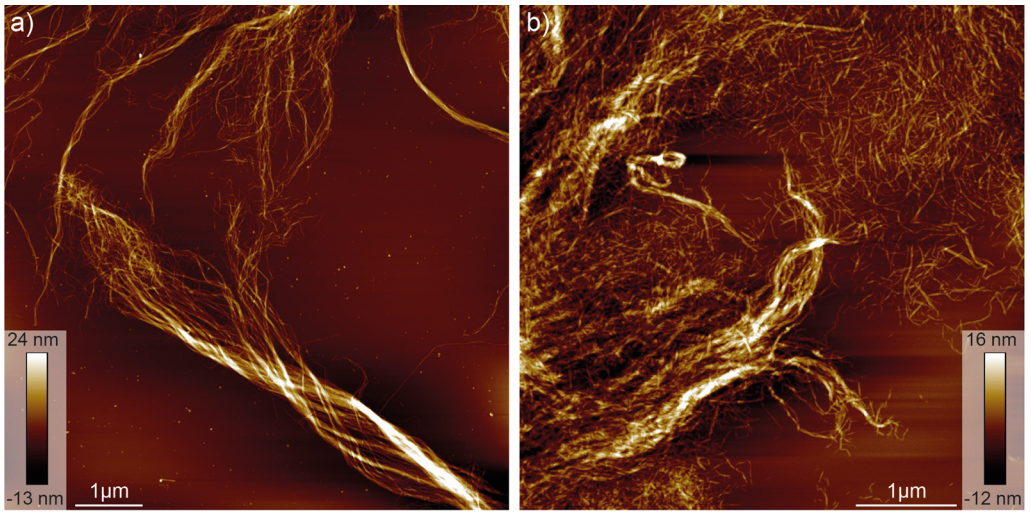

Figure 1. Unbleached and bleached softwood pulp after TEMPO-mediated oxidation. AFM images of (a) unbleached and (b) bleached pulp after TEMPO-mediated oxidation without further treatment.

Dynamic Light Scattering (DLS). The translational diffusion coefficient was determined by DLS using a Zetasizer. To minimize particle interactions, the CNF dispersion was diluted (0.1 g/L) below the overlap concentration (~0.3 g/L) and centrifuged at 12000 RCF for 30 min to remove large agglomerates potentially present in the samples. Each sample was measured three times, while a measurement consists of 10−20 runs, determined by the device. The fibril length L was calculated, assuming that the fibrils behave as rigid rods and using eq 1:[38,39]

$$D = \frac{kT}{3\pi\eta L}\left(\ln L - \ln d + c_0 + \frac{c_1 d}{L} + \frac{c_2 d^2}{L^2}\right) \quad (1)$$

where D is the translational diffusion coefficient measured by DLS, k is the Boltzmann's constant, T is the temperature (25 °C), η is the viscosity of water, d is the fibril diameter determined by AFM or WAXS, and c_0, c_1, and c_2 are constants (0.312, 0.565 and 0.1, respectively) for cylindrical objects, taken from ref 38.

RESULTS AND DISCUSSION

Effects of Varying Charge Density on Fibrillization of TEMPO-Mediated Oxidized Cellulose Nanofibrils. After the TEMPO-mediated oxidation at pH 10 under the same conditions, the industrially bleached and unbleached softwood pulp showed different morphologies. As observed in Figure 1, the unbleached pulp (a) revealed generally long fibers that unravel into fibril bundles and eventually single fibrils, whereas the bleached pulp (b) consisted of a fibril network with less pronounced hierarchical levels. The reason for the difference may be related to the composition of the pulps as discussed in the next paragraph. In both pulp samples, the smallest fibrils revealed a height of around 1.3 nm, whereas fibrils with diameters around 4−5 nm were the most represented population (Figure S1).

The surface charges of the T-CNF, present as carboxylic groups, was determined by conductivity titration of dispersed oxidized softwood pulp. Figure 2a indicates a difference in efficiency of the oxidation process between unbleached and beforehand industrially bleached softwood pulp as source material. The charge density of the fibrils from bleached pulp increased from 270 μmol/g CNF (1.5 mmol NaClO) up to 1120 μmol/g CNF (10 mmol NaClO), whereas the unbleached pulp from 150 μmol/g CNF (1.5 mmol NaClO) up to 940 μmol/g CNF (10 mmol NaClO). The difference between bleached and unbleached pulp is justified by the different compositions of the two genitor sources. The unbleached pulp still contains lignin and hemicellulose, which then would be removed in the following industrial bleaching process.[40] One of the bleaching agents used in this process is NaClO that is also the primary oxidant of the TEMPO-mediated oxidation. Therefore, the presence of lignin makes NaClO less available for the TEMPO-mediated oxidation, decreasing the overall efficiency of the cellulose oxidation process for the unbleached pulp.[41] Additionally, hemicellulose present in the unbleached pulp is also oxidized at the primary OH groups and, due to its good water dispersibility, it is removed during the rinsing process, which further decreases the efficiency of the TEMPO-mediated oxidation reaction.

The fibrillization was promoted by ultrasonication and facilitated due to the repulsion between the single fibrils within the fibril bundles. The repulsion resulted from the negative surface charges of the fibrils at neutral pH. The resulting single CNFs after centrifugation can be observed in the AFM images in Figure 2c−f, where large agglomerates can be found for the lowest charge density sample after 7 min of sonication (c). With increasing charge density (d−f), fewer fibril agglomerates were observed, translating, in turn, to an increased single fibril yield at constant sonication time. Statistical analysis of the images reveals a decrease in length-weighted average fibril length from 670 to 340 nm and 880 to 470 nm, while increasing the concentration of oxidation agent from 1.5 to 10 mmol/g of cellulose for CNF from bleached and unbleached pulp, respectively (Figure 2b). Analysis of the unfibrillated fibrils fraction revealed (Figure S2) similar fibril network structures as those found in the not sonicated pulp seen in Figure 1. Since it was not possible to extract individual fibril parameters from these sample fractions, they were not further analyzed.

Indeed, a breakdown of fibrils into shorter objects with increasing charge density can be expected when the electrostatic energy per unit length (which favors breaking) exceeds the cohesive energy per unit length:

$$\frac{k_B T l_B (N_{charges})^2}{L} > \sigma\pi D_{equivalent} L + \Delta F \cdot L \quad (2)$$

DOI: 10.1021/acs.biomac.8b01706
Biomacromolecules 2019, 20, 1288−1296

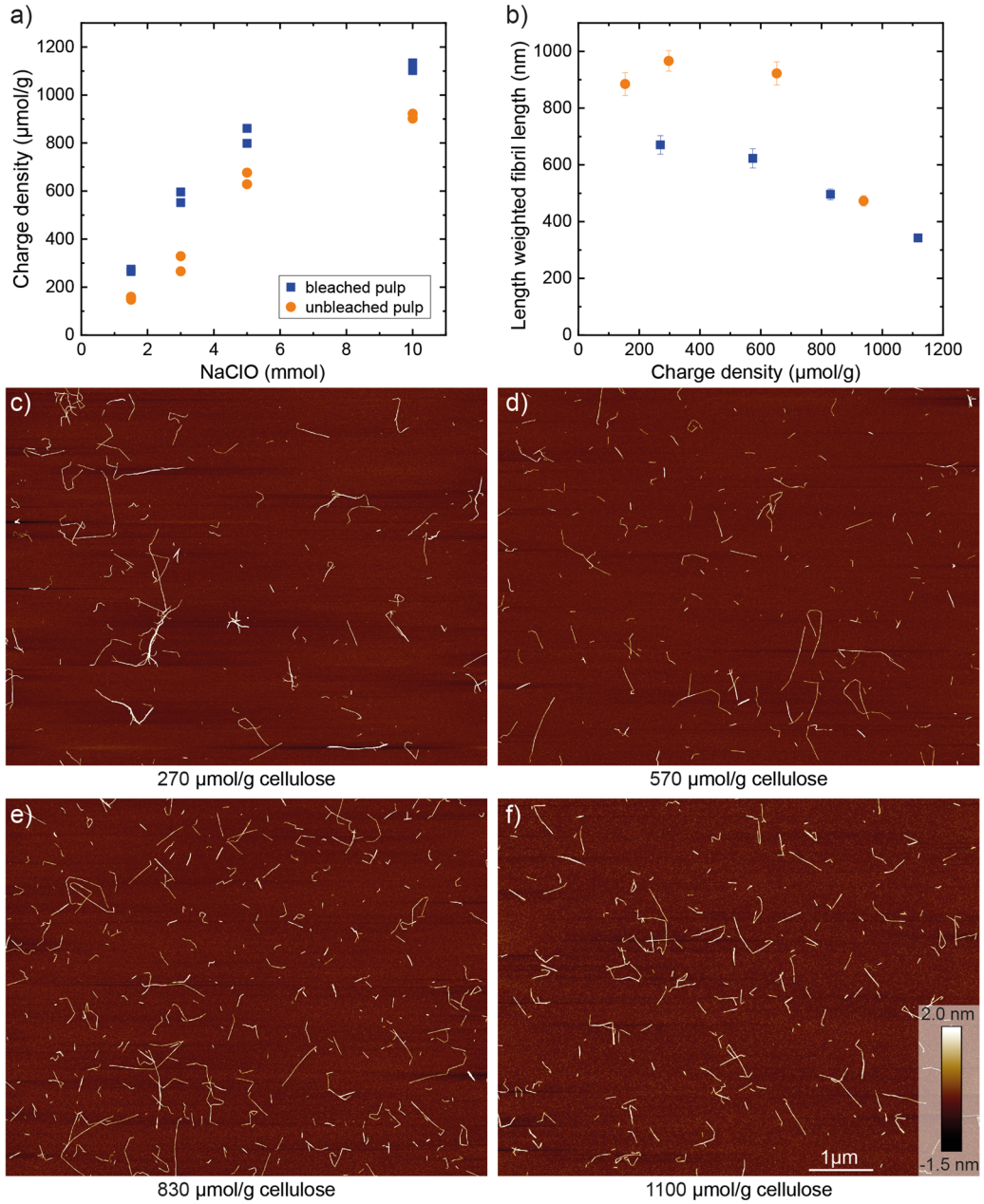

Figure 2. Influence of charge density on the fibril length. (a) Charge density of carboxylic acid groups induced by varying amounts of NaClO added per gram of bleached (blue squares) and unbleached (orange circles) softwood pulp (including data points from two independent measurements). (b) Plot of the length weighted averaged fibril contour length vs charge density for CNFs prepared from bleached (blue squares) and unbleached (orange circles) wood pulps after 7 min of sonication (with error bars expressing the standard error of the mean, $n > 200$). (c–f) AFM images of T-CNF produced from bleached softwood pulp with varying charge densities after 7 min of sonication. The scale and height bars in image (f) apply to all AFM images.

where k_B is the Boltzmann constant, T is the temperature, l_B is the Bjerrum length, $N_{charges}$ is the total number of charges per length L, σ is the fibril–water interfacial tension, $\pi D_{equivalent}$ is the cross-sectional perimeter of the fibril ($D_{equivalent}$ being the diameter of the cylindrical fibril with an equivalent cross-sectional perimeter) and ΔF is the total cohesive energy per length L holding the single CNF together.[42] The critical linear charge density, at which the electrostatic breakdown is expected, can be extracted from eq 2 using the definition $\lambda_{critic} = N_{charges}/L$, thus

$$\lambda_{critic}^2 > \frac{\sigma\pi D_{equivalent} + \Delta F}{k_B T l_B} \quad (3)$$

Due to the high polydispersity of the fibril length and the presence of many short fragments, the difference between samples was more evident using the length weighted average fibril length. This trend is also in agreement with earlier reported data.[21] However, a plateau in fibril length could be observed for fibrils produced from the unbleached source at charge densities between 150 and 650 μmol/g, in general agreement with eq 3 and indicating that a certain threshold of repulsion is needed for an efficient fibrillization by sonication.

DOI: 10.1021/acs.biomac.8b01706
Biomacromolecules 2019, 20, 1288–1296

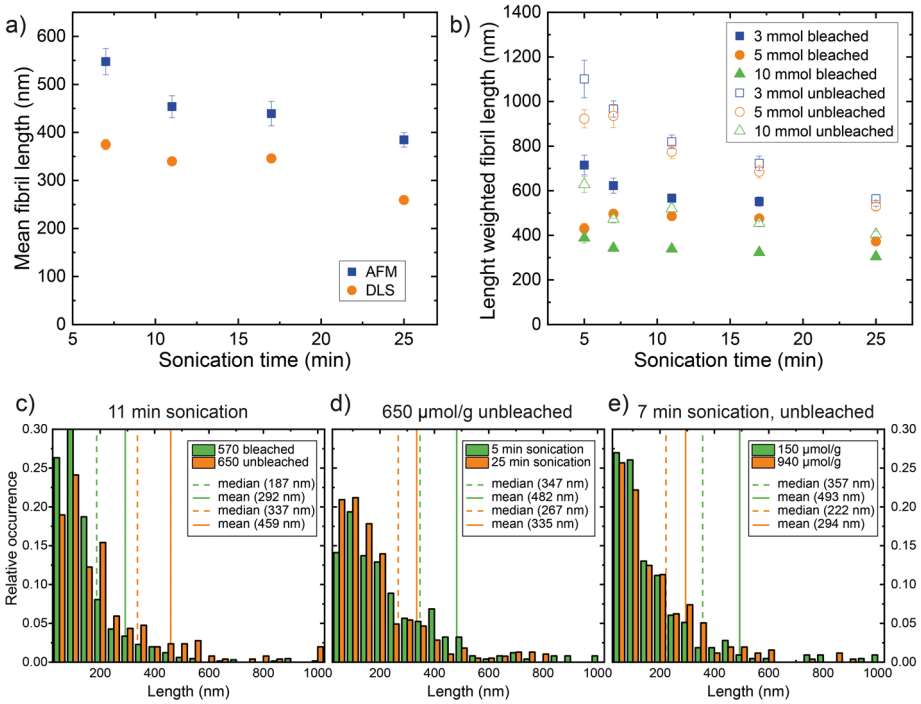

Figure 3. Influence of sonication time on fibril length. (a) Comparison of mean fibril length between DLS (orange circle) and AFM (blue square) measurements of CNF dispersions prepared from unbleached wood pulp with a charge density of 300 μmol/g CNF (standard deviation of DLS of 3 measurements and standard error of AFM $n > 200$). (b) Length weighted fibril length determined by fibril tracking from AFM images (error bars express the standard error of the mean, $n > 200$) for different sonication times. (c) Length distribution of CNF from bleached and unbleached pulp at constant sonication time (11 min) and similar charge density. (d) Length distribution of CNF with different sonication time (5 and 25 min) with constant charge density and pulp. (e) Length distribution of CNF with varying charge density (150 and 940 μmol/g) from unbleached pulp after 7 min sonication.

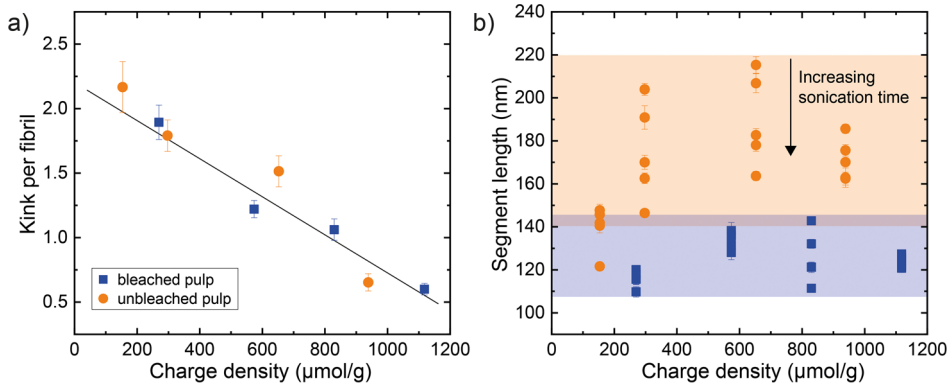

Figure 4. Influence of charge density (a) on the average number of kinks per fibril after 7 min of sonication (with the black line as a linear fit) and (b) the segment length at different sonication times, where the colored areas indicate the average segment length of the samples from unbleached and bleached pulps. For both graphs, the standard error is calculated based on the data of more than 200 tracked fibrils per point.

Impact of Sonication Time on Fibril Length. In agreement with earlier reports, not only the charge density, but also the sonication time, has a direct impact on the fibril length.[23,24] A comparison of the ensemble average mean fibril length obtained by DLS (Figure 3a), using eq 1, with the average contour height based on fibril tracking data from AFM images or based on deconvolution of the WAXS pattern showed good agreement, supporting the use of the fibril-based contour tracking method (Figure S3). This method is hereafter used throughout the manuscript. The analysis revealed the expected shortening due to sonication. The weighted length of the longest unbleached fibrils (3 mmol unbleached) possessed the lowest charge density and decreased from 1100 nm after 5 min of sonication to 560 nm after 25 min of sonication (Figure 3b). Samples with higher charge density (e.g., 10 mmol unbleached) that had generally shorter fibril lengths after 5 min of sonication, exhibited less shortening and seemed, after 25 min, to converge to a similar length such as the 3 mmol unbleached CNFs. The fibrils from the bleached source were generally shorter than those from the unbleached (Figure 3c). Starting at 720 nm after 5 min of sonication, the length of 3 mmol bleached fibrils declined to 540 nm after 25 min of sonication. Finally, the highest charged, bleached fibrils did not significantly change in length with additional sonication after the initial 5 min. A screening of sonication times shorter than 5 min revealed an inefficient fibrillization, and huge agglomerates

DOI: 10.1021/acs.biomac.8b01706
Biomacromolecules 2019, 20, 1288−1296

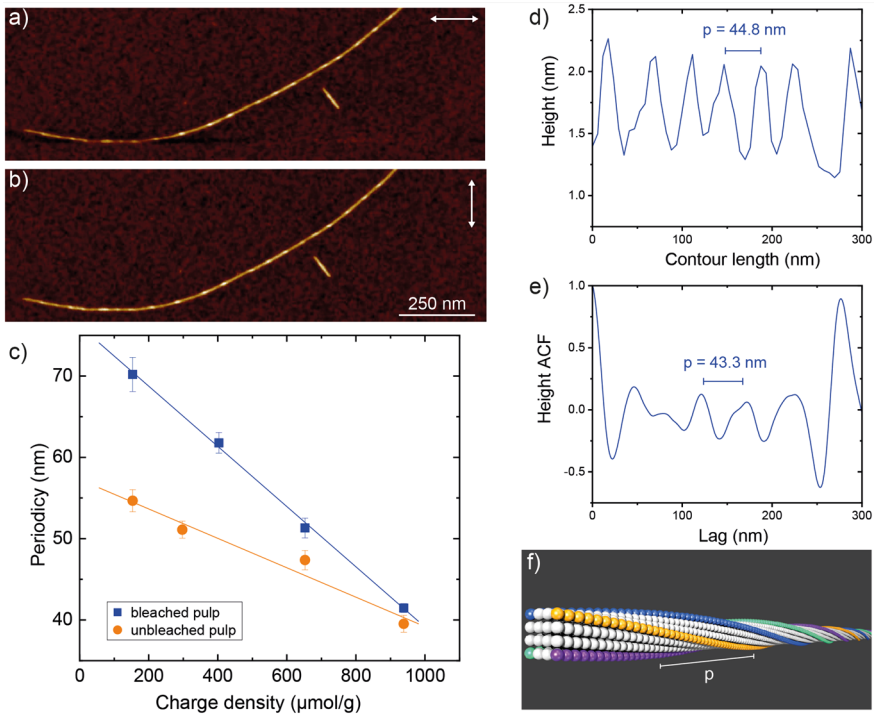

Figure 5. Analysis of the periodicity of the pitch of cellulose fibrils. (a) AFM image of a single fibril (unbleached source after 11 min of sonication), where the white line indicates the scanning direction. (b) AFM image of the same fibril with 90° turned scanning direction. (c) Dependency of periodicity on the charge density of CNFs from bleached (blue square) and unbleached (orange circle) softwood pulp sources, with the respective linear fit. (d) Height plot along the contour of a single fibril. (e) Plot of the height autocorrelation function (ACF) vs lag of the same fibril contour. (f) Schematic of a twisted 4 × 4-cross section fibril, where the periodicity p is indicated.

were still observed by the AFM analysis, whereas only a few single fibrils were present (Figure S4). Since the CNFs produced with 1.5 mmol NaClO per gram of cellulose have nearly the same length as those with 3 mmol NaClO per gram of cellulose, they are not shown in the plot, but the measured values are listed in Table S1. The existence of a threshold of minimal length with increasing sonication time was observed earlier[24] and seems to be mainly dependent on the cellulose source. Figure 3c–e shows a comparison of the length distributions obtained when varying one parameter while keeping the other parameters constant.

Nyström et al. proposed a mechanism for cutting and hence shortening of fibrils, where fibrils break not only at the kink position but along rigid segments too, possibly via an intermediate kink forming step.[23] These results suggested that the kink zones are regions formed from mechanical defects, thereby being mechanically weaker than the rigid segments. Moreover, that same study showed that acid hydrolysis may be used to shorten fibrils preferentially at positions of kinks. Thus, in order to obtain fibrils with strong mechanical strength and chemical resilience for further applications, it is desirable to minimize the number of kinks, while maintaining a maximum fibril length.

Influence of Surface Charge Density on Kink Density and Segment Length. So far, we can conclude that increasing charge density as well as sonication time decreases the fibril length. Do both these treatments also affect the morphology of the single fibrils in a similar way? To find out, we continued the analysis with a focus on the number of kinks per fibril and the segment length of the differently charged samples. Figure 4a suggests that, with increasing charge densities, the average number of kinks per fibril is linearly decreasing from 1.9 to 0.6 and from 2.2 to 0.7 kinks per fibril for bleached and unbleached CNF, respectively. The amount of kinks per fibrils seems to be independent of the cellulose source. Therefore, the effect of increasing charge density is comparable with increasing sonication time, both leading to fewer kinks. Analyzing the average segment lengths in Figure 4b indicates an average segment length between 110 and 145 nm and 140 and 220 nm for bleached and unbleached fibrils, respectively.

Connecting the dependence of the fibril length from the charge density with the finding of the maximal segment length, we can conclude that the fibrils from the unbleached source with a charge density of 650 μmol/g CNF result in the optimal properties of high aspect ratio and a low density of kinks.

Periodicity and Twist of CNFs as a Function of Fibril Charge and Thickness. AFM imaging provides an accurate measurement in z-direction. These z-data yield precise topological information on the height variations along the fibril contour, thus, allowing us to extract information on the pitch of the fibrils. Figure 5a,b shows a representative example of a CNF scanned in orthogonal directions, where the right-handedness of the fibril is directly observable in both images. Figure 5c shows the twist periodicity, p, of the fibrils (measured as the average distance between two consecutive height maxima along the fibril contour, as depicted in Figure 5d) as a function of increasing fibril charge density. The periodicity of fibrils from bleached and unbleached sources linearly decreased from 70 to 41 nm and 55 to 40 nm, respectively, with increasing charge density. The autocorrelation function (ACF) implemented in FiberApp[36] provides an alternative way to determine the periodicity, as shown in Figure 5e. The height profile in Figure 5d shows an average

DOI: 10.1021/acs.biomac.8b01706
Biomacromolecules 2019, 20, 1288–1296

relative height difference between minima and maxima of $\sim 2^{1/2}$, suggesting a squared cross section for the right-handed fibrils as illustrated schematically in Figure 5f and in agreement with previous works[19,34,43] but significantly different from the observations of microfibrils that have a wider (10−50 nm) rectangular cross-section.[25] Based on the squared cross section and the ensued periodicity, we can assume the length of the pitch as $L = 4p$ and obtain values between 158 and 281 nm.

Turning to the fibril height, we note slight differences in fibril height based on the AFM analysis as well as the WAXS fitting; however, these variations are not significant (Figure S5). The average height of all tracked fibrils was 1.7 ± 0.2 nm, in agreement with previous results.[19,44,45] Further, height differences of less than the size of a glucose molecule (ca. 0.5 nm) are difficult to justify but can result from averaging the heights within the sample population. Moreover, with increasing charge density, the roughness of the mica surface is also increased and might influence the determination of the height (Figure S6). The increase in roughness originates from an increasing amount of flexible polymers, either residual hemicellulose that was not completely removed in the preceding treatment or due to peeling-off of cellulose polymer chains from the fibril surface by sonication.

It is expected that the fibril height has a large influence, through its quartic relation to the torsional stiffness of the fibrils, on the equilibrium twisted fibril configuration, as supported also by theoretical works.[28,29] When electrostatics are also taken into account, the fibril twist undergoes a more complex behavior. For amyloid fibrils, it has been shown that the twist periodicity is a function of the electrostatic strength and can be accurately described by a model balancing the twist elasticity of the fibril with the electrostatic repulsion from the fibril surface charges.[46,47] Assuming a similar mechanism for the present CNFs, their twist periodicity should decrease for an increasing amount of electrostatic charge as a result of an increased electrostatic torsional momentum, which is indeed what we observed, as shown in Figure 5c, for both the bleached and unbleached fibrils. These results confirm unambiguously that the average linear charge density of the fibrils regulates contour length and twist periodicity and, thus, has a very strong impact on the final morphology of CNFs.

CONCLUSIONS

The present study provides insights into the nanostructure of single CNFs resulting from a systematic variation of both chemical and physical parameters, that is, the industrial treatment of the pulp starting material, the amount of oxidant in the TEMPO-mediated oxidation process, and the mechanical treatment (sonication). Using AFM imaging and statistical image analysis, we observed a principal difference in fibrillization between samples from bleached and unbleached softwood pulp, where the unbleached fibrils were generally less charged but longer. However, the length of the individual fibril largely depends on the charge density induced by the TEMPO-mediated oxidation and the sonication time used to fibrillate the samples. Increasing these two parameters leads to shorter and thinner fibrils. We found an optimum between maximal fibril length and minimal number of kinks at a charge density of around 600 μmol/g after 11 min of sonication.

Furthermore, AFM imaging allowed us to resolve the twisting periodicity of individual CNFs. We found a decreasing twist periodicity of the fibrils for increasing charge density. This is in agreement with a model balancing the twist elasticity of the fibrils with the electrostatic repulsion from the fibril charges.[46,47]

ASSOCIATED CONTENT

Supporting Information

The Supporting Information is available free of charge on the ACS Publications website at DOI: 10.1021/acs.biomac.8b01706.

Figure S1: Morphology differences of bleached and unbleached pulp. Figure S2: Morphology of pellet from centrifugation of bleached and unbleached pulp. Figure S3: Comparison of mean fibril length from DLS using fibril height values from AFM and WAXS. Figure S4: AFM images showing the influence of increasing sonication time. Figure S5: Plotted height of fibrils from different sources versus charge density. Figure S6: Differences in roughness on APTES-modified mica caused by polymer covering. Figure S7: Impact of APTES-modified mica versus no modification on length distribution and twist periodicity. Figure S8: Typical WAXS profile of bleached CNF. Table S1: Measured parameters for different fibril samples. Table S2: Crystallinity data from WAXS. Table S3: Yield after sonication and centrifugation. List with used materials, chemicals and instruments (PDF).

AUTHOR INFORMATION

Corresponding Authors

*E-mail: raffaele.mezzenga@hest.ethz.ch.
*E-mail: gustav.nystroem@empa.ch.

ORCID

Mario Arcari: 0000-0002-9055-6525
Raffaele Mezzenga: 0000-0002-5739-2610
Gustav Nyström: 0000-0003-2739-3222

Author Contributions

M.A. and G.N. designed the study. M.A., E.Z., R.A., J.A., and A.S.F. performed the experiments. All authors analyzed data. M.A., R.M., and G.N. wrote the paper.

Notes

The authors declare no competing financial interest.

ACKNOWLEDGMENTS

We thank Domsjö, Sweden, for providing the softwood pulp, Kathleen Smith for critical reading and discussing the manuscript, and Mattia Usuelli for sharing his knowledge about light scattering. M.A. and G.N. acknowledge funding from the Swiss National Science Foundation Ambizione Grant No. PZ00P2_168023/1.

REFERENCES

(1) Moon, R. J.; Martini, A.; Nairn, J.; Simonsen, J.; Youngblood, J. Cellulose Nanomaterials Review: Structure, Properties and Nanocomposites. *Chem. Soc. Rev.* **2011**, *40*, 3941−3994.

(2) Kontturi, E.; Laaksonen, P.; Linder, M. B.; Nonappa; Gröschel, A. H.; Rojas, O. J.; Ikkala, O. Advanced Materials through Assembly of Nanocelluloses. *Adv. Mater.* **2018**, *30*, 1703779.

(3) Engström, A. C.; Ek, M.; Henriksson, G. Improved Accessibility and Reactivity of Dissolving Pulp for the Viscose Process: Pretreatment with Monocomponent Edoglucanase. *Biomacromolecules* **2006**, *7*, 2027−2031.

(4) Henriksson, M.; Henriksson, G.; Berglund, L. A.; Lindström, T. An Environmentally Friendly Method for Enzyme-Assisted Prepara-

DOI: 10.1021/acs.biomac.8b01706
Biomacromolecules 2019, 20, 1288−1296

tion of Microfibrillated Cellulose (MFC) Nanofibers. *Eur. Polym. J.* **2007**, *43*, 3434−3441.
(5) Pääkkö, M.; Ankerfors, M.; Kosonen, H.; Nykänen, A.; Ahola, S.; Österberg, M.; Ruokolainen, J.; Laine, J.; Larsson, P. T.; Ikkala, O.; et al. Enzymatic Hydrolysis Combined with Mechanical Shearing and High-Pressure Homogenization for Nanoscale Cellulose Fibrils and Strong Gels. *Biomacromolecules* **2007**, *8*, 1934−1941.
(6) Saito, T.; Kimura, S.; Nishiyama, Y.; Isogai, A. Cellulose Nanofibers Prepared by TEMPO-Mediated Oxidation of Native Cellulose. *Biomacromolecules* **2007**, *8*, 2485−2491.
(7) Fujisawa, S.; Okita, Y.; Fukuzumi, H.; Saito, T.; Isogai, A. Preparation and Characterization of TEMPO-Oxidized Cellulose Nanofibril Films with Free Carboxyl Groups. *Carbohydr. Polym.* **2011**, *84*, 579−583.
(8) Shimizu, M.; Saito, T.; Isogai, A. Water-Resistant and High Oxygen-Barrier Nanocellulose Films with Interfibrillar Cross-Linkages Formed through Multivalent Metal Ions. *J. Membr. Sci.* **2016**, *500*, 1−7.
(9) Benítez, A. J.; Walther, A. Cellulose Nanofibril Nanopapers and Bioinspired Nanocomposites: A Review to Understand the Mechanical Property Space. *J. Mater. Chem. A* **2017**, *5*, 16003−16024.
(10) Saito, T.; Uematsu, T.; Kimura, S.; Enomae, T.; Isogai, A. Self-Aligned Integration of Native Cellulose Nanofibrils towards Producing Diverse Bulk Materials. *Soft Matter* **2011**, *7*, 8804−8809.
(11) Kobayashi, Y.; Saito, T.; Isogai, A. Aerogels with 3D Ordered Nanofiber Skeletons of Liquid-Crystalline Nanocellulose Derivatives as Tough and Transparent Insulators. *Angew. Chem., Int. Ed.* **2014**, *53*, 10394−10397.
(12) Zhang, Z.; Sèbe, G.; Rentsch, D.; Zimmermann, T.; Tingaut, P. Ultralightweight and Flexible Silylated Nanocellulose Sponges for the Selective Removal of Oil from Water. *Chem. Mater.* **2014**, *26*, 2659−2668.
(13) Nyström, G.; Marais, A.; Karabulut, E.; Wågberg, L.; Cui, Y.; Hamedi, M. M. Self-Assembled Three-Dimensional and Compressible Interdigitated Thin-Film Supercapacitors and Batteries. *Nat. Commun.* **2015**, *6*, 7259.
(14) Okita, Y.; Saito, T.; Isogai, A. Entire Surface Oxidation of Various Cellulose Microfibrils by TEMPO-Mediated Oxidation. *Biomacromolecules* **2010**, *11*, 1696−1700.
(15) Sacui, I. A.; Nieuwendaal, R. C.; Burnett, D. J.; Stranick, S. J.; Jorfi, M.; Weder, C.; Foster, E. J.; Olsson, R. T.; Gilman, J. W. Comparison of the Properties of Cellulose Nanocrystals and Cellulose Nanofibrils Isolated from Bacteria, Tunicate, and Wood Processed Using Acid, Enzymatic, Mechanical, and Oxidative Methods. *ACS Appl. Mater. Interfaces* **2014**, *6*, 6127−6138.
(16) Jiang, F.; Han, S.; Hsieh, Y. Lo. Controlled Defibrillation of Rice Straw Cellulose and Self-Assembly of Cellulose Nanofibrils into Highly Crystalline Fibrous Materials. *RSC Adv.* **2013**, *3*, 12366−12375.
(17) Hiraoki, R.; Ono, Y.; Saito, T.; Isogai, A. Molecular Mass and Molecular-Mass Distribution of TEMPO-Oxidized Celluloses and TEMPO-Oxidized Cellulose Nanofibrils. *Biomacromolecules* **2015**, *16*, 675−681.
(18) Li, Q.; Renneckar, S. Supramolecular Structure Characterization of Molecularly Thin Cellulose I Nanoparticles. *Biomacromolecules* **2011**, *12*, 650−659.
(19) Usov, I.; Nyström, G.; Adamcik, J.; Handschin, S.; Schütz, C.; Fall, A.; Bergström, L.; Mezzenga, R. Understanding Nanocellulose Chirality and Structure-Properties Relationship at the Single Fibril Level. *Nat. Commun.* **2015**, *6*, 7564.
(20) Hirota, M.; Tamura, N.; Saito, T.; Isogai, A. Oxidation of Regenerated Cellulose with NaClO2 Catalyzed by TEMPO and NaClO under Acid-Neutral Conditions. *Carbohydr. Polym.* **2009**, *78*, 330−335.
(21) Shinoda, R.; Saito, T.; Okita, Y.; Isogai, A. Relationship between Length and Degree of Polymerization of TEMPO-Oxidized Cellulose Nanofibrils. *Biomacromolecules* **2012**, *13*, 842−849.
(22) Battista, O. A. Hydrolysis and Crystallization of Cellulose. *Ind. Eng. Chem.* **1950**, *42*, 502−507.
(23) Nyström, G.; Arcari, M.; Adamcik, J.; Usov, I.; Mezzenga, R. Nanocellulose Fragmentation Mechanisms and Inversion of Chirality from the Single Particle to the Cholesteric Phase. *ACS Nano* **2018**, *12*, 5141−5148.
(24) Saito, T.; Kuramae, R.; Wohlert, J.; Berglund, L. A.; Isogai, A. An Ultrastrong Nanofibrillar Biomaterial: The Strength of Single Cellulose Nanofibrils Revealed via Sonication-Induced Fragmentation. *Biomacromolecules* **2013**, *14*, 248−253.
(25) Hanley, S.; Revol, J.-F.; Godbout, L.; Gray, D. Atomic Force Microscopy and Transmission Electron Microscopy of Cellulose from Micrasterias Denticulata; Evidence for a Chiral Helical Microfibril Twist. *Cellulose* **1997**, *4*, 209−220.
(26) Khandelwal, M.; Windle, A. Origin of Chiral Interactions in Cellulose Supra-Molecular Microfibrils. *Carbohydr. Polym.* **2014**, *106*, 128−131.
(27) Elazzouzi-Hafraoui, S.; Nishiyama, Y.; Putaux, J.-L.; Heux, L.; Dubreuil, F.; Rochas, C. The Shape and Size Distribution of Crystalline Nanoparticles Prepared by Acid Hydrolysis of Native Cellulose. *Biomacromolecules* **2008**, *9*, 57−65.
(28) Matthews, J. F.; Skopec, C. E.; Mason, P. E.; Zuccato, P.; Torget, R. W.; Sugiyama, J.; Himmel, M. E.; Brady, J. W. Computer Simulation Studies of Microcrystalline Cellulose Iβ. *Carbohydr. Res.* **2006**, *341*, 138−152.
(29) Paavilainen, S.; Rog, T.; Vattulainen, I. Analysis of Twisting of Cellulose Nanofibrils in Atomistic Molecular Dynamics Simulations. *J. Phys. Chem. B* **2011**, *115*, 3747−3755.
(30) Zhao, Z.; Shklyaev, O. E.; Nili, A.; Mohamed, M. N. A.; Kubicki, J. D.; Crespi, V. H.; Zhong, L. Cellulose Microfibril Twist, Mechanics, and Implication for Cellulose Biosynthesis. *J. Phys. Chem. A* **2013**, *117*, 2580−2589.
(31) Bu, L.; Himmel, M. E.; Crowley, M. F. The Molecular Origins of Twist in Cellulose I-Beta. *Carbohydr. Polym.* **2015**, *125*, 146−152.
(32) Hadden, J. A.; French, A. D.; Woods, R. J. Unraveling Cellulose Microfibrils: A Twisted Tale. *Biopolymers* **2013**, *99*, 746−756.
(33) Kannam, S. K.; Oehme, D. P.; Doblin, M. S.; Gidley, M. J.; Bacic, A.; Downton, M. T. Hydrogen Bonds and Twist in Cellulose Microfibrils. *Carbohydr. Polym.* **2017**, *175*, 433−439.
(34) Ciesielski, P. N.; Matthews, J. F.; Tucker, M. P.; Beckham, G. T.; Crowley, M. F.; Himmel, M. E.; Donohoe, B. S. 3D Electron Tomography of Pretreated Biomass Informs Atomic Modeling of Cellulose Microfibrils. *ACS Nano* **2013**, *7*, 8011−8019.
(35) Schütz, C.; Van Rie, J.; Eyley, S.; Gençer, A.; van Gorp, H.; Rosenfeldt, S.; Kang, K.; Thielemans, W. Effect of Source on the Properties and Behavior of Cellulose Nanocrystal Suspensions. *ACS Sustainable Chem. Eng.* **2018**, *6*, 8317−8324.
(36) Usov, I.; Mezzenga, R. FiberApp: An Open-Source Software for Tracking and Analyzing Polymers, Filaments, Biomacromolecules, and Fibrous Objects. *Macromolecules* **2015**, *48*, 1269−1280.
(37) Korten, T.; Nitzsche, B.; Gell, C.; Ruhnow, F.; Leduc, C.; Diez, S. Fluorescence Imaging of Single Kinesin Motors on Immobilized Microtubules. *Methods Mol. Biol.* **2011**, *783*, 121−137.
(38) de la Torre, J. G.; Bloomfield, V. A. Hydrodynamic Properties of Complex, Rigid, Biological Macromolecules: Theory and Applications. *Q. Rev. Biophys.* **1981**, *14*, 81−139.
(39) Nordenström, M.; Fall, A.; Nyström, G.; Wågberg, L. Formation of Colloidal Nanocellulose Glasses and Gels. *Langmuir* **2017**, *33*, 9772−9780.
(40) Hubbe, M. A.; Rojas, O. J.; Lucia, L. A. Green Modification of Surface Characteristics of Cellulosic Materials at the Molecular or Nano Scale : A Review. *BioResources* **2015**, *10*, 6095−6206.
(41) Okita, Y.; Saito, T.; Isogai, A. TEMPO-Mediated Oxidation of Softwood Thermomechanical Pulp. *Holzforschung* **2009**, *63*, 529−535.
(42) Dehsorkhi, A.; Castelletto, V.; Hamley, I. W.; Adamcik, J.; Mezzenga, R. The Effect of PH on the Self-Assembly of a Collagen Derived Peptide Amphiphile. *Soft Matter* **2013**, *9*, 6033.
(43) Atalla, R. H.; Atalla, R. S.; Agarwal, U. P. The Nanostructures of Native Celluloses, Their Transformations upon Isolation, and Their

DOI: 10.1021/acs.biomac.8b01706
Biomacromolecules 2019, 20, 1288−1296

Implications for Production of Nanocelluloses. *ACS Symp. Ser.* **2017**, *1251*, 1−18.
(44) Leppänen, K.; Andersson, S.; Torkkeli, M.; Knaapila, M.; Kotelnikova, N.; Serimaa, R. Structure of Cellulose and Microcrystalline Cellulose from Various Wood Species, Cotton and Flax Studied by X-Ray Scattering. *Cellulose* **2009**, *16*, 999−1015.
(45) Daicho, K.; Saito, T.; Fujisawa, S.; Isogai, A. The Crystallinity of Nanocellulose: Dispersion-Induced Disordering of the Grain Boundary in Biologically Structured Cellulose. *ACS Appl. Nano Mater.* **2018**, *1*, 5774−5785.
(46) Assenza, S.; Adamcik, J.; Mezzenga, R.; De Los Rios, P. Universal Behavior in the Mesoscale Properties of Amyloid Fibrils. *Phys. Rev. Lett.* **2014**, *113*, 268103.
(47) Adamcik, J.; Mezzenga, R. Adjustable Twisting Periodic Pitch of Amyloid Fibrils. *Soft Matter* **2011**, *7*, 5437−5443.

DOI: 10.1021/acs.biomac.8b01706
Biomacromolecules 2019, 20, 1288−1296